Electron and wave characteristics observed by the THEMIS satellites near the magnetic equator during a pulsating aurora

A. Nakajima,[1,2] K. Shiokawa,[1] K. Sakaguchi,[1,3] Y. Miyoshi,[1] S. Lee,[1] V. Angelopoulos,[4] O. Le Contel,[5] J. P. McFadden,[6] J. W. Bonnell,[6] K.-H. Fornacon,[7] and E. Donovan[8]

Received 10 August 2011; revised 29 December 2011; accepted 23 January 2012; published 16 March 2012.

[1] Based on conjugate ground and THEMIS satellite observations, we show electron spectra and wave characteristics near the magnetic equatorial plane during a pulsating aurora event on the high latitude side of the auroral oval. The pulsating aurora was observed by a 30-Hz sampled all-sky imager (ASI) at Gillam (56.4°N, 265.4°E), Canada, at ∼0840-0910 UT on 8 January 2008. The auroral intensity pulsation at the possible THEMIS D (THD) footprints had frequency peaks at ∼0.1–0.2 Hz. The footprint of THD was in the poleward part of the proton aurora observed by a meridian-scanning photometer. After auroral pulsation began at ∼0842 UT, both THD and THEMIS E which was near THD in the mid-tail at 11.6–11.8 R_E, observed enhanced field-aligned electron fluxes at energies of 1–10 keV. However, the amplitudes of whistler mode waves and electrostatic cyclotron harmonics (ECH) waves observed by THD with the highest sampling rate of 8 kHz were not significant, showing a marked contrast to the recent report of clear correlation between whistler mode waves and auroral pulsations observed at 5–9 R_E. We suggest that the observed field-aligned electrons, which are probably caused by Fermi-type acceleration associated with earthward plasma flow in the mid-tail plasma sheet, are modulated by some wave processes to cause pulsating auroras.

Citation: Nakajima, A., et al. (2012), Electron and wave characteristics observed by the THEMIS satellites near the magnetic equator during a pulsating aurora, *J. Geophys. Res.*, *117*, A03219, doi:10.1029/2011JA017066.

1. Introduction

[2] Pulsating aurora, a quasiperiodic auroral phenomenon with a typical period of ∼0.5–20 s, is usually observed extensively in the midnight and morning sectors during the substorm recovery phase. The pulsating patches have irregular shapes with typical dimensions of ∼10–200 km [e.g., *Royrvik and Davis*, 1977; *Oguti*, 1978; *Yamamoto*, 1988]. Rocket and satellite measurements indicate that auroral pulsations are manifestations of modulation of precipitating high-energy electrons with energies from a few keV to 100 keV [e.g., *Sandahl et al.*, 1980; *Sato et al.*, 2002].

[3] Several authors have suggested that during pulsating auroras, high-energy electrons are supplied by pitch angle scattering through whistler wave-particle interactions near the magnetosphere's equatorial plane [e.g., *Tsuruda et al.*, 1981; *Johnstone*, 1983; *Davidson*, 1990; *Nemzek et al.*, 1995; *Li et al.*, 2011a, 2011b]. In this scenario, it is expected that electrons will be scattered into the two loss cones symmetrically in the magnetosphere and precipitate into both hemispheres, resulting in pulsating aurora with north-south phase conjugacy. Using interhemispheric conjugate observations, *Fujii et al.* [1987] showed that the patchy-type pulsating aurora appears nearly simultaneously in both hemispheres. According to recent studies, however, the conjugacy of pulsating auroras is generally poor in shape and phase [e.g., *Minatoya et al.*, 1995; *Sato et al.*, 2004; *Watanabe et al.*, 2007], a result that is inconsistent with the above traditional picture for the pulsating auroras. *Sato et al.* [2004] estimated the altitude of the electron modulation for a pulsating aurora using the time-of-flight (TOF) method of electron energy-dispersion observed by the FAST satellite. They concluded that, an electron modulation occurs near the earth, far from the equatorial plane, and that some unknown process in the magnetosphere-ionosphere coupling system plays an important role in modulation of pulsating auroras. *Miyoshi et al.* [2010] applied a TOF method, which includes propagation of whistler waves, to the REIMEI satellite data. Using a model calculation, they concluded that the wave-

[1]Solar-Terrestrial Environment Laboratory, Nagoya University, Japan.
[2]Now at Japan Science and Technology Agency, Tokyo, Japan.
[3]Now at National Institute of Information and Communications Technology, Koganei, Japan.
[4]Institute of Geophysics and Planetary Physics, University of California, Los Angeles, CA, USA.
[5]Laboratoire de Physique des Plasmas, CNRS-Ecole Polytechnique-UPMC, Palaiseau, France.
[6]Space Sciences Laboratory, University of California, Berkeley, CA, USA.
[7]Institut für Geophysik und Meteorologie, Technical University of Braunschweig, Braunschweig, Germany.
[8]Department of Physics and Astronomy, University of Calgary, Alberta, Canada.

0148-0227/12/2011JA017066

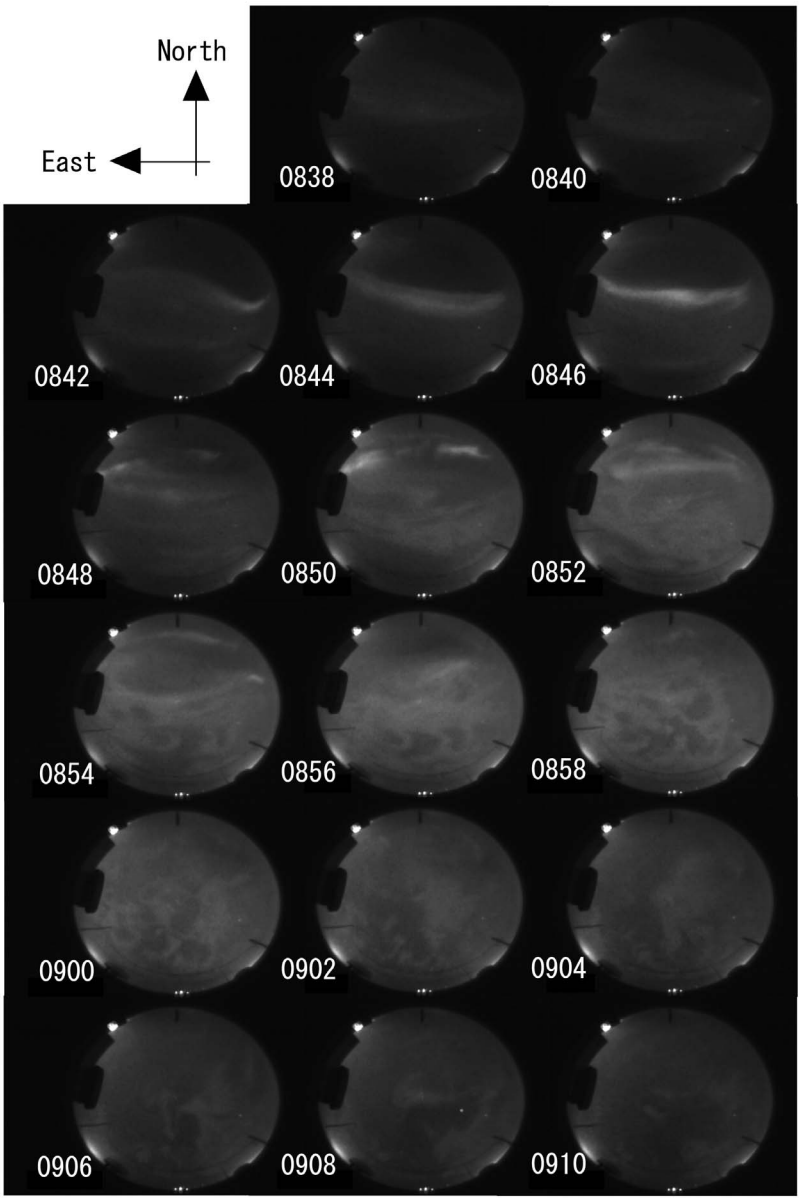

Figure 1. White-light auroral images obtained by an all sky imager (ASI) at Gillam every 2 min from 0838 to 0910 UT on 8 January 2008. The top and left sides of the images are to the north and east, respectively.

particle interaction region can still be in the equatorial plane if one considers field-aligned propagation of whistler chorus waves with a rising tone. Considering the TOF model of *Miyoshi et al.* [2010] and *Nishiyama et al.* [2011] tried to estimate whistler mode wave frequencies near the modulation region of the pulsating aurora using the REIMEI satellite data; and the results are consistent with the statistical distribution of whistler mode chorus waves.

[4] Most of these previous studies of pulsating auroras have been based on observations near the ionosphere, using radar and optical measurements on the ground, rocket, and low-altitude satellites, and some combinations of these observational methods. Since magnetic mapping from the magnetosphere to the conjugate point in the ionosphere can contain significant ambiguity, it is difficult to directly compare magnetospheric measurements to particular pulsation patches. After discussing this mapping problem, *Nemzek et al.* [1995] compared the plasma density and energetic electron flux variations at geosynchronous orbit to pulsating auroras observed by an optical instrument on the ground.

[5] *Nishimura et al.* [2010, 2011] showed a conjugate observation of pulsating auroras by a ground all-sky camera and by the Time History of Events and Macroscale Interactions during Substorms (THEMIS) satellites at 5–9 R_E. They show a very clear correlation between the pulsating auroral intensity observed on the ground and lower-band chorus intensity observed by the THEMIS-A satellite at the equatorial plane of the magnetosphere, indicating that the

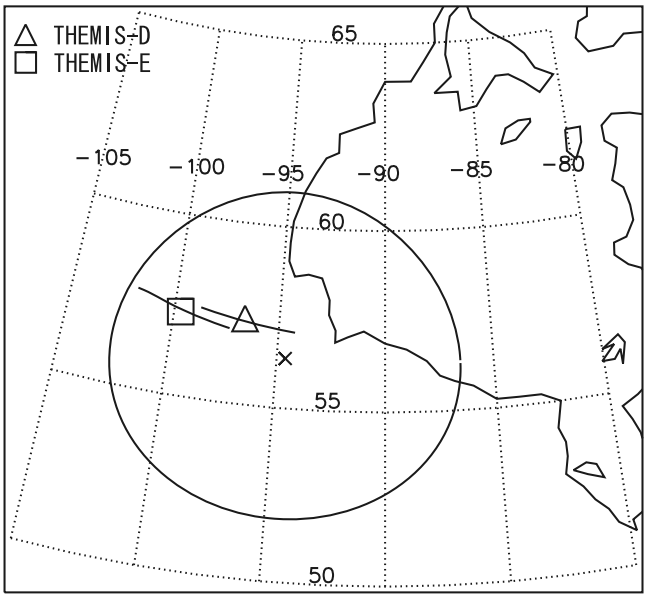

Figure 2. Field of view of ASI at Gillam (cross) with a radius of 500 km, corresponding to a zenith angle of ∼80° at an auroral altitude of 100 km. Footprints of THEMIS-D (THD) and -E (THE) at an altitude of 100 km at 0853 UT on 8 January 2008 are indicated by the triangle and the square, respectively. The solid curves show satellite tracks of THD and THE from 0835 to 0910 UT. These footprints were calculated using the T96_01 geomagnetic field model [*Tsyganenko*, 1995, 1996].

temporally-modulated lower-band chorus produces pulsating auroras. *Liang et al.* [2010] also compared the ground observations of pulsating auroral structures with THEMIS satellite data. They suggested that electron cyclotron harmonic (ECH) waves play a key role in pitch angle diffusion of plasma sheet electrons, which causes pulsating aurora and the modulation of ECH waves by ultralow-frequency (ULF) waves causes macroscopic structures of the pulsating auroras. THEMIS ground and satellite observations make such conjugate measurements of pulsating auroras possible. Such measurements are still very limited, however. Pulsating auroras appear at various local times and latitudes at all substorm phases from initial to recovery. Not one but several production mechanisms may cause auroral intensity modulation. High-time resolution of less than 1 s is often necessary to detect pulsating auroras; the nominal sampling rate of THEMIS all-sky imagers is 3 s.

[6] In this paper, we report another case study of a pulsating auroral event using a high-time resolution (30 Hz) ground all-sky imager (ASI) and THEMIS satellites at 11.6–11.8 R_E, much more tailward than those reported by *Nishimura et al.* [2010, 2011]. When the ASI in the Canadian auroral region observed pulsating auroras in the post-midnight sector on 8 January 2008, the footprints of two THEMIS satellites in the mid-tail plasma sheet were mapped in the field of view (FoV) of the ASI. However, the observed wave powers of whistler and ECH are rather small and correspondence between wave activity and pulsation is insignificant. We discuss these observations in the context of the possible cause of pulsating auroras.

2. Observations

2.1. Data Set

[7] We had a campaign of auroral observations using white-light ASIs with an FoV of 180° and a sampling rate of 30 Hz at two Canadian stations in the auroral zone during a THEMIS-ground conjunction interval from 2–15 January 2008 [*Shiokawa et al.*, 2009]. The observation sites were Gillam (56.4°N, 265.4°E, dipole geomagnetic latitude (MLAT): 65.6°) and Fort Smith (60.0°N, 248.1°E, MLAT: 67.0°). In this study, we use ASI data obtained at Gillam on 8 January 2008.

[8] During the campaign interval, ionospheric footprints of the THEMIS satellites passed through the FoV of the ASI at Gillam in the post-midnight sector where pulsating auroras are frequently observed [e.g., *Royrvik and Davis*, 1977]. The THEMIS mission consists of five satellites launched into the magnetosphere on 17 February 2007 [*Angelopoulos et al.*, 2008]. Each was equipped with comprehensive in-situ particle and field instruments. In the present study, we use particle and field data obtained by the solid state telescope (SST), electrostatic analyzer (ESA) [*McFadden et al.*, 2008], fluxgate magnetometer (FGM) [*Auster et al.*, 2008], search coil magnetometer (SCM) [*Roux et al.*, 2008], and electric field instrument (EFI) [*Bonnell et al.*, 2008].

[9] During the campaign, the ASI at Gillam observed pulsating auroras on 8, 12, 13, and 14 January, 2008. In this paper, we focus on the pulsating auroral event observed on 8 January 2008, because during this pulsating auroral event two THEMIS satellites were in the FoV of the ASI and observed particles and fields with the highest-time resolution.

2.2. Overview

[10] On 8 January 2008, auroral pulsations were observed by the ASI at Gillam at magnetic local times (MLTs) of ∼2–5 h from ∼0840 to 1200 UT. In Figure 1, white-light images obtained by the ASI at 0838-0910 UT (∼2 h MLT) are displayed every 2 min. The auroral luminosity with an arc-like structure along the east-west direction was faintly observed in the center of the image at 0838-0840 UT. As shown by *Sakaguchi et al.* [2009], auroral substorm onset took place at ∼0830 UT on 8 January 2008 at Fort Smith, which is located west of Gillam. In Figure 1, a clear auroral arc appear from the west at ∼0842 UT. This clear auroral arc probably expanded from the west associated with the substorm onset observed at Fort Smith.At ∼0842-0850 UT, the auroral emission expanded over the whole FoV of the ASI at Gillam.

[11] Although auroral emission pulsations cannot be identified in the snapshot images in Figure 1, the emissions with patchy structures seen after 0848 UT showed clear pulsations in the FoV of ASI at Gillam except for the auroral arc in the northern sky. The weak auroral pulsations had already started over lower half in the images from ∼0842 UT. The luminosity of the pulsations became more active at

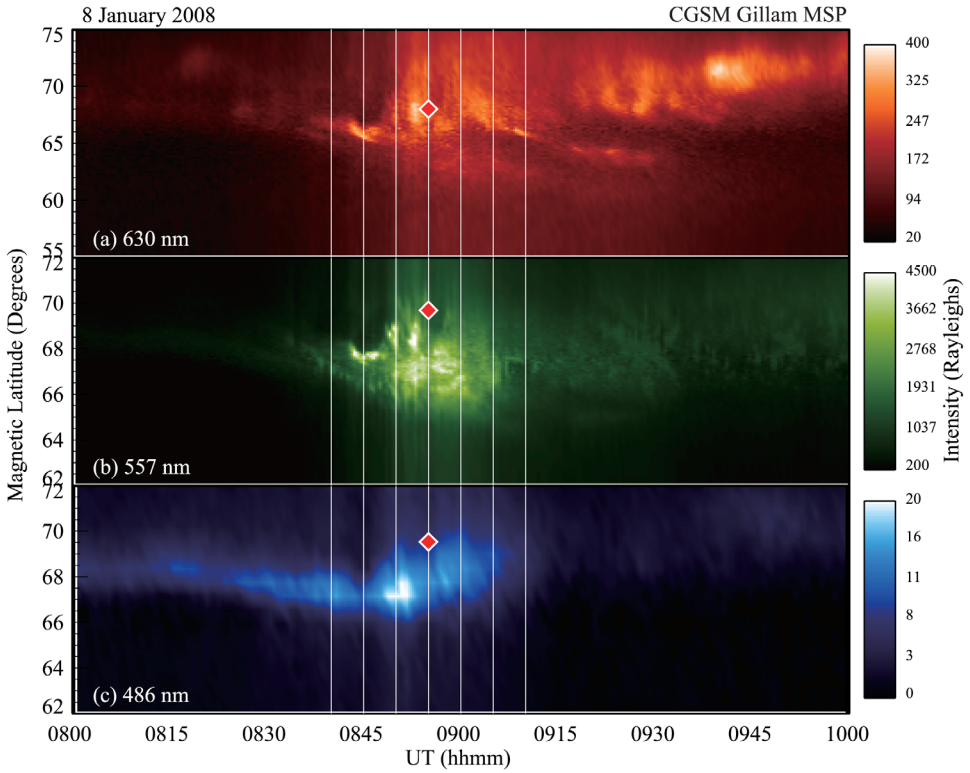

Figure 3. North-south cross sections (keograms) of auroral intensities at wavelengths of (a) 630.0 nm, (b) 557.7 nm, and (c) 486.1 nm observed by a meridian-scanning photometer at Gillam, Canada, on 8 January 2008. The vertical white lines are every 5 min at 0840-0910 UT. The red rectangles indicate the footprints of THD at 0855 UT.

~0848 UT. The active pulsations over the whole FoV lasted from ~0850 to 0904 UT; the auroral arc was observed in the northern part of the FoV until ~0854 UT. From 0900 UT onwards, the intensity of these pulsating auroras gradually decreased. However, weak pulsating patches were found in the whole FoV until 0910 UT in the last image of Figure 1. These weak pulsations had been observed with gradually-decreasing luminosity until ~1200 UT.

[12] For the pulsating aurora event in Figure 1, we compare the ASI data at Gillam with plasma and field observations by the THEMIS-D (THD) and THEMIS-E (THE) satellites in the magnetosphere. The circle in the map in Figure 2 shows the FoV of ASI at Gillam with a radius of 500 km, corresponding to a zenith angle of ~80° at an auroral altitude of 100 km. The triangle (58.2°N, 262.4°E) and the square (58.3°N, 259.5°E) are the footprints of THD and THE, respectively, at 0853 UT on 8 January 2008, when the electron fluxes observed by THD were most intense, as shown later. The footprints of both THD and THE move westward in the FoV of ASI along the solid curves from 0835 to 0910 UT. The footprint of THD is closer to Gillam (cross in the map) than that of THE.

[13] Figure 3 shows the auroral activities at wavelengths of 630.0 nm, 557.7 nm, and 486.1 nm observed by a meridian-scanning photometer at Gillam during this event. Associated with the substorm onset at ~0830 UT, the stable auroral arc brightened at ~68 MLAT and expanded both equatorward and poleward. The auroral intensity was not as large as typical substorm auroras. The footprint of THD at 0855 UT, indicated by the red rectangles, was located poleward of the brightening aurora in all the three wavelengths. The auroral intensity gradually decreases after 0900 UT, showing many patchy structures particularly in the 557.7-nm keogram.

[14] Figure 4 shows locations of THD (triangle) and THE (square) at 0853 UT on 8 January 2008 in the X-Y (Figure 4, top) and X-Z (Figure 4, bottom) planes in GSM coordinates. The locations at 0853 UT were THD: (−9.4, −6.5, −3.1) R_E and THE: (−9.6, −5.6, −3.3) R_E in GSM coordinates. These satellite locations are at 11.6–11.8 R_E in the mid-tail, very different from the locations in work by *Nishimura et al.* [2010, 2011], 5–9 R_E. THD was on the magnetic field lines indicated by the solid curves, which were calculated using the geomagnetic field model (T96_01) by *Tsyganenko* [1995, 1996]. The difference in two satellite locations was ~1 R_E from 0835 to 0910 UT. Both THD and THE were located in the post midnight sector near the magnetic equatorial plane.

[15] The footprints and magnetic field lines in Figures 2 and 4 are calculated using the T96_01 geomagnetic field model [*Tsyganenko*, 1995, 1996]. Footprint mapping using magnetic field model contains uncertainty, however. We also calculated the field-line mapping using the TS04 model. The difference between the footprints in T96 and TS04 is less than 0.1 degree for both latitudes and longitudes. This is probably because the revisions of the Tsyganenko models after T96 were mainly for the inner magnetosphere, including ring current and storm effects, whereas the THEMIS

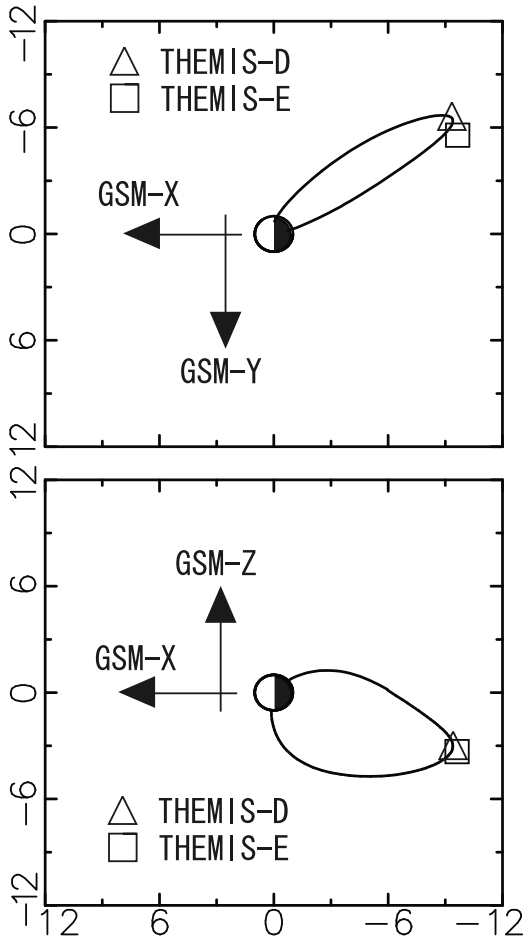

Figure 4. Locations of THD (triangle) and THE (square) at 0853 UT on 8 January 2008 in (top) X-Y and (bottom) X-Z planes in GSM coordinates. The solid curves indicate the magnetic field lines connected to the THD location at 0853 UT. The field lines are calculated using the geomagnetic field model (T96_01) [*Tsyganenko*, 1995, 1996].

satellite in the present event was in the outer magnetosphere in the tail.

[16] Global magnetic field variations during substorms can also affect the field-line mapping calculation. The present pulsating auroral event took place after a substorm onset. To check the mapping accuracy, we compared magnetic field intensities observed by THD and THE with those from the T96_01 geomagnetic field model at these satellite locations. The total magnetic field intensities at 0853 UT from FGM onboard the THD and THE were 15.5 nT and 21.8 nT, respectively. The total intensities from the T96_01 model at 0853 UT were 13.8 nT and 13.5 nT at the THD and THE locations, respectively. At the THD location, differences between the observation and the model were less than 3 nT, not only for the total intensity but also for x-, y-, and z-components of magnetic field. In addition, the direction of these magnetic field components was the same in both the observation and the model for THD. On the other hand, the total magnetic field difference between the observation and the model for THE was much larger (>8 nT) and the direction of x-component was opposite. Thus, the field-line mapping of THE to the ground may contain significant ambiguity. THE can also be located near the conjugate point of the pulsating aurora, since the pulsating auroras were observed in a wide area in the ASI FoV of Gillam. In this paper, we mainly compare THD observations with ground ASI observations.

[17] Figure 5a is auroral keogram obtained by taking a cross section in the north-south meridian of auroral images at 262.4°E, where the THD footprint was located at 0853 UT. Latitudes of the THD footprint are indicated by the dashed line in this keogram. The bottom panels of Figure 5 show the THD particle and field data. In Figure 5b, the X and Z components of the magnetic field in the GSM coordinates are plotted by the blue and red curves, respectively. Figure 5c shows ion velocity measured by ESA along the GSM-X direction. Energy-time (E-T) spectrograms of omnidirectional electrons with energies of 30–600 keV (Figure 5d) and 30 eV–30 keV (Figure 5e) are produced by SST and ESA, respectively. The ESA measurement with the highest time resolution (3 s) was done from 0843 to 0903 UT, as shown in Figure 5e. The pitch angle distributions of electrons at energies of 0.5–30 keV obtained by ESA are shown in Figure 5f. Figures 5g and 5h show wave amplitudes at 1–4000 Hz in electric and magnetic fields measured by EFI and SCM, respectively, produced by Filter Bank (FBK), which calculates amplitudes of band-pass filtered waves for 6 frequencies at 2.3 Hz, 9.1 Hz, 36 Hz, 140 Hz, 570 Hz, and 2.69 kHz, onboard. The two black curves in Figures 5g and 4h indicate electron cyclotron frequency (f_{ce}, higher frequency) and lower hybrid resonance frequency (f_{lhr}, lower frequency).

[18] Figures 6a–6h which are in the same format as Figures 5a–5h, are an auroral keogram and the data from THE, which was located about ~1 R_E west of THD. Figure 6a shows an auroral keogram obtained by taking a cross section in the north-south meridian of auroral images at 259.5°E where the THE footprint was located at 0853 UT. The THE-ESA measurement with the highest time resolution (3 s) was made from ~0838 to 0908 UT, as shown in Figures 6e and 6f.

[19] Auroral emissions expanded to higher and lower latitudes after ~0848 UT in Figures 5a and 6a. The auroral pulsations were observed mainly in the lower-latitude side of the keogram. However, higher-latitude auroras also show pulsations after 0850 UT. Associated with the appearance of the auroral arc at ~0841-0848 UT, magnetic field dipolarization characterized by a decreasing X-component and an increasing Z-component started at 0846 UT (0842 UT) at THD (THE) in Figure 5b (Figure 6b). Earthward ion flows over 100 km/s are observed by THD at 0849 UT and by THE at 0844 UT in Figures 5c and 6c, respectively. These substorm signatures at THE were earlier than those at THD, probably because THE was closer to the onset meridian near midnight, as shown in Figure 4.

[20] After substorm onset, flux enhancements of plasma sheet electrons with energies from a few hundred eV to a few hundred keV were observed in Figures 5d, 5e, 6d, and 6e. The electron fluxes with energies of 0.5–30 keV are most intense in field-aligned upward and downward directions for the plotted interval in Figures 5f and 6f. The flux intensity of these bidirectional beams varies significantly.

[21] In Figures 5g, 5h, 6g, and 6h, enhanced waves are detected at frequencies below 100 Hz, mainly below f_{lhr}

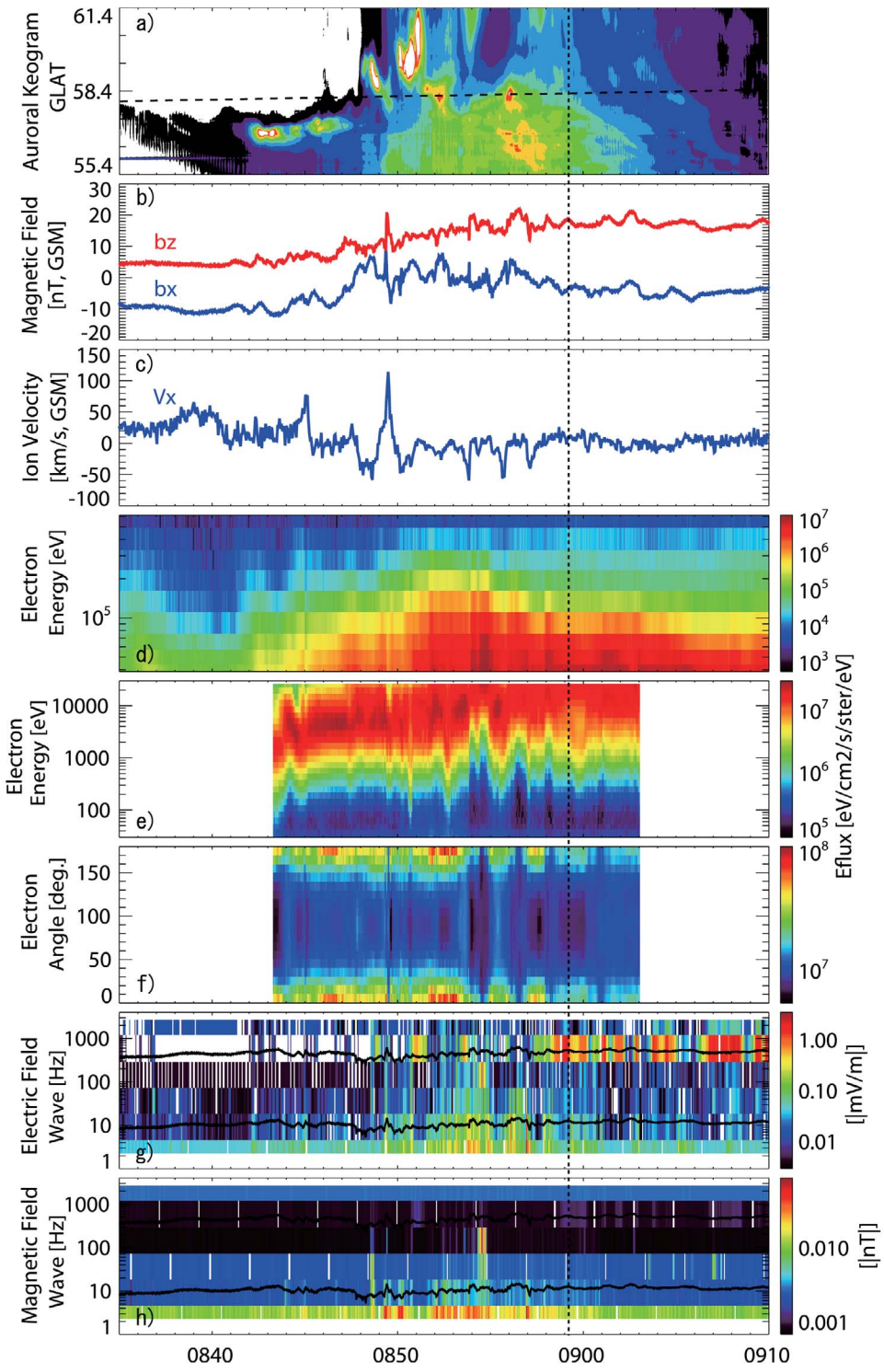

Figure 5. (a) Auroral keogram (cross section) for the north-south meridian at 262.4°E (longitude of THD footprint) from 0835 to 0910 UT on 8 January 2008. (b) Magnetic field (X and Z components), (c) ion velocity in the X direction, energy-time (E-T) spectrograms of (d) 30–600 keV and (e) 30 eV–30 keV, (f) pitch angle distributions of electrons with energies of 0.5–30 keV, and wave spectrograms of (g) electric field and (h) magnetic field, observed by THD. In Figure 5a, latitude of the THD footprint is indicated by the dashed line. In each panel of Figures 5g and 5h, electron cyclotron frequency (f_{ce}) and lower hybrid resonance frequency (f_{lhr}) are shown by the upper and lower black curves, respectively. The vertical dashed line denotes the time when wave observations with the highest time resolution were performed by THD, as shown in Figure 11.

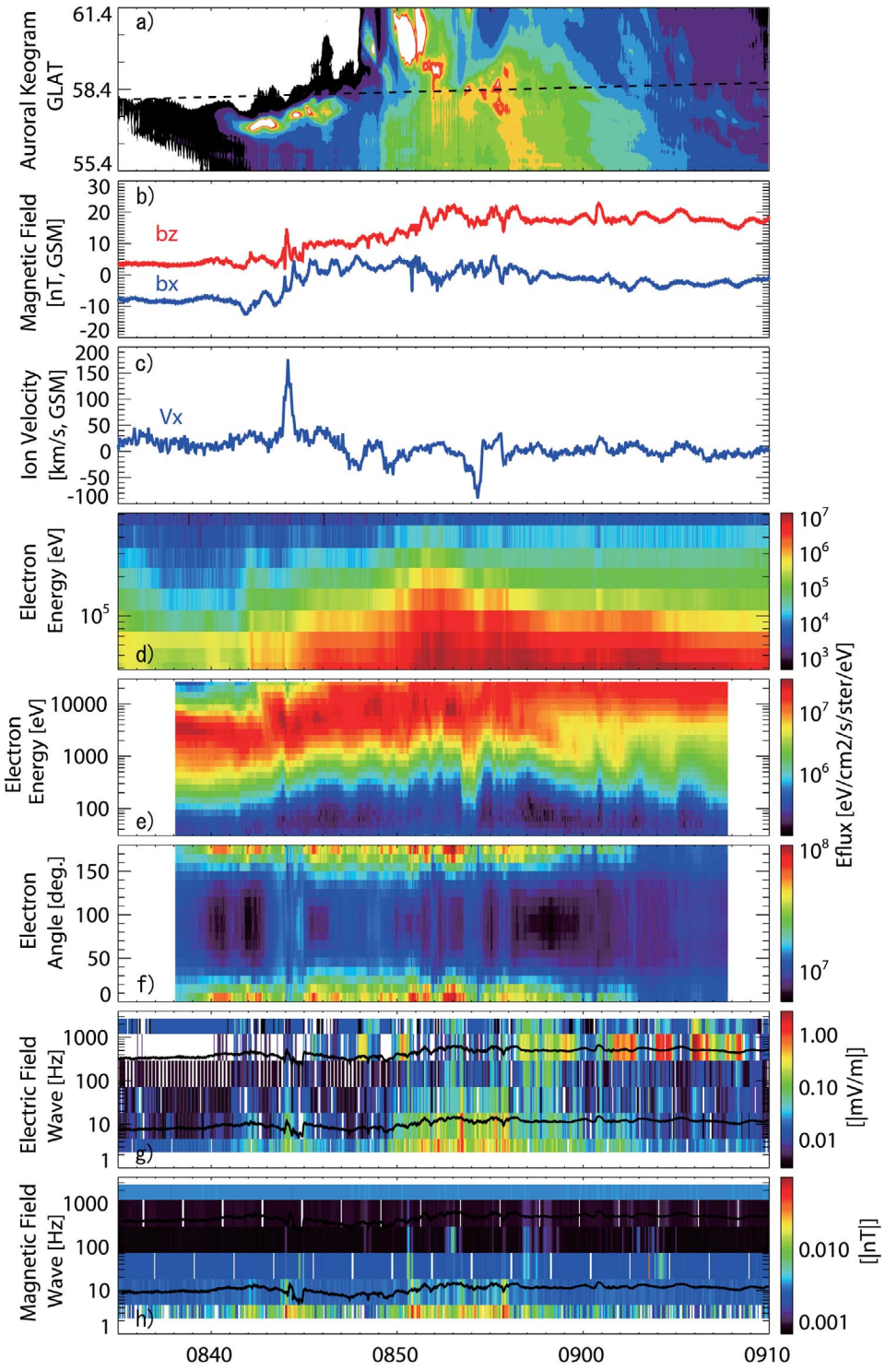

Figure 6. (a) Auroral keogram (cross section) for the north-south meridian at 259.5°E (longitude of THE footprint) during 0835-0910 UT on 8 January 2008. (b) Magnetic field (X and Z components), (c) ion velocity in the X direction, energy-time (E-T) spectrograms of (d) 30–600 keV and (e) 30 eV–30 keV, (f) pitch angle distributions of electrons with energies of 0.5–30 keV, and wave spectrograms of (g) electric field and (h) magnetic field observed by THE. In Figure 6a, the latitude of the THE footprint is indicated by the dashed line. In each panel of Figures 6g and 6h, electron cyclotron frequency (f_{ce}) and lower hybrid resonance frequency (f_{lhr}) are shown by the upper and lower black curves, respectively.

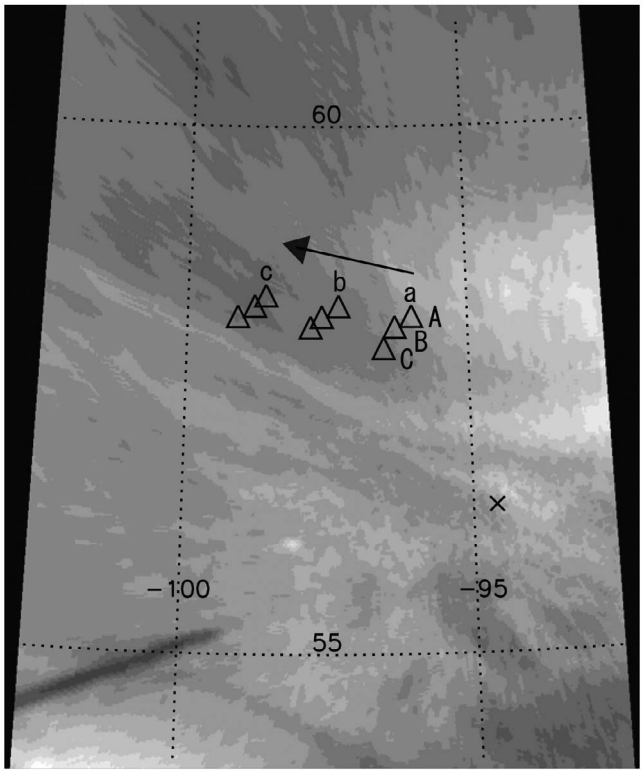

Figure 7. An auroral image mapped to an altitude of 100 km from the original all-sky image at Gillam (cross in the map) at 0853 UT on 8 January 2008. The top and left sides of the images correspond to north and west, respectively. Based on T96_01 geomagnetic field model [*Tsyganenko*, 1995, 1996], footprints of THD (triangles) at 0843, 0853, and 0903 UT are shown with a, b, and c, respectively. The footprint of THD moves westward along the arrow. The footprints denoted A, B, and C indicate footprint locations calculated for IMF-Bz of −0.3 nT, −1.3 nT (actual value), and −2.3 nT, respectively.

(∼10 Hz). The start of such waves at 0849 UT (THD) and at 0844 UT (THE) is associated with the intense ion flows in Figures 5c and 6c. Higher frequency waves with a discrete frequency from 300 to 1000 Hz near the f_{ce} were also enhanced only in the electric field data in Figures 5g and 6g, indicating that these higher-frequency waves are electrostatic. The higher-frequency waves become more intense after ∼0856 UT. The discrete wave is probably the electrostatic cyclotron harmonic (ECH) wave.

2.3. Auroral Intensity, Electron Flux, and Wave Activities

[22] Next, we compare the electron flux and wave activities observed by THD with the auroral intensity observed by ASI at the footprints of THD. Figure 7 shows an auroral image at 0853 UT mapped to the 100-km altitude from the original all-sky image at Gillam. The THD footprints shown by triangles, are estimated at (a) 0843 UT, (b) 0853 UT, and (c) 0903 UT, which are the start, center, and end times of the highest time resolution of ESA measurements shown in Figure 5e. The footprints are calculated using three values of the interplanetary magnetic field (IMF) Bz, i.e., (A) −0.3 nT, (B) −1.3 nT (actual value), and (C) −2.3 nT in the T96_01 model.

[23] The footprints move westward from 0843 to 0903 UT, as indicated by the arrow. The footprint variations are 0.5° in latitude and 3.1° in longitude for the nine footprints for temporal and IMF-Bz changes. The auroral patches are seen in the east and south of these nine footprints in this image. The patches sometimes extend into the footprint locations according to the pulsation.

[24] In Figure 8, auroral luminosities at the nine footprints in Figure 7 are compared with the electron-energy flux and wave spectra observed by THD. Figures 8d–8f present auroral intensities (counts) at A-C, respectively, from 0843 to 0903 UT. In each panel, black, red and blue curves indicate counts at footprints for selected times a-c (0843, 0853, and 0903 UT), respectively. Wave spectra in the magnetic and electric fields measured by THD are shown in Figures 8b and 8c, respectively. The integrated wave power in the magnetic field is shown in Figure 8a. The electron energy flux of field-aligned downward (0°–20°), perpendicular (80°–100°), and field-aligned upward (160°–180°) obtained by THD is plotted in Figures 8g–8i, respectively. In these panels, the energy flux is colored according to the electron energy (black: 0.5–1 keV; blue: 1–5 keV; green: 5–10 keV; red: 10–30 keV).

[25] Auroral intensity variations at the nine footprints show similar structures in Figures 8d–8f. The field-aligned electron fluxes in Figures 8g and 8i are much larger than the perpendicular flux in Figure 8h. The field-aligned electron fluxes tend to be large when the auroral intensity is large at 0849-0850 UT and 0852-0853 UT. When auroral intensity fluctuated significantly in Figures 8d–8f (e.g., ∼0849 and ∼0852 UT), field-aligned electron flux also fluctuated in Figures 8g and 8i. For all pairs, we calculated correlation coefficients between the auroral intensities and the electron fluxes. The highest correlation coefficients (0.5–0.6) were obtained for the pairs between the intensity at point A at 0843 UT and the 5–10 keV and 10–30 keV parallel and anti-parallel electron fluxes and between the intensity at point B at 0843 UT and the 10–30 keV parallel and anti-parallel electron fluxes. These correlations between the electron fluxes and auroral intensities suggest that the THD is located near the conjugate point of the observed pulsating aurora. The electron energy ranges of the highest correlation at 5–10 keV and 10–30 keV are the typical energy ranges that cause pulsating aurora.

[26] In Figures 8b and 8c, the wave features are clearer in the electric field data. ECH waves are intermittently observed as discrete high-frequency enhancement at ∼600–700 Hz. The whistler mode waves below 100 Hz are also enhanced at ∼0850-0856 UT. A positive correlation between these waves and the field-aligned electron fluxes is not seen, however. Indeed, the ECH waves at ∼600–700 Hz tend to show a negative correlation with the field-aligned electron fluxes. The magnetic field wave power in Figure 8a tends to increase when the auroral intensity and field-aligned electron flux increases at 0849 UT, 0853 UT, and 0856 UT. This integrated wave power comes mainly from waves at frequencies below 10 Hz.

[27] The typical period of pulsating aurora is ∼0.5–20 s [e.g., *Royrvik and Davis*, 1977; *Oguti*, 1978; *Yamamoto*, 1988]. To check the frequency of both the auroral

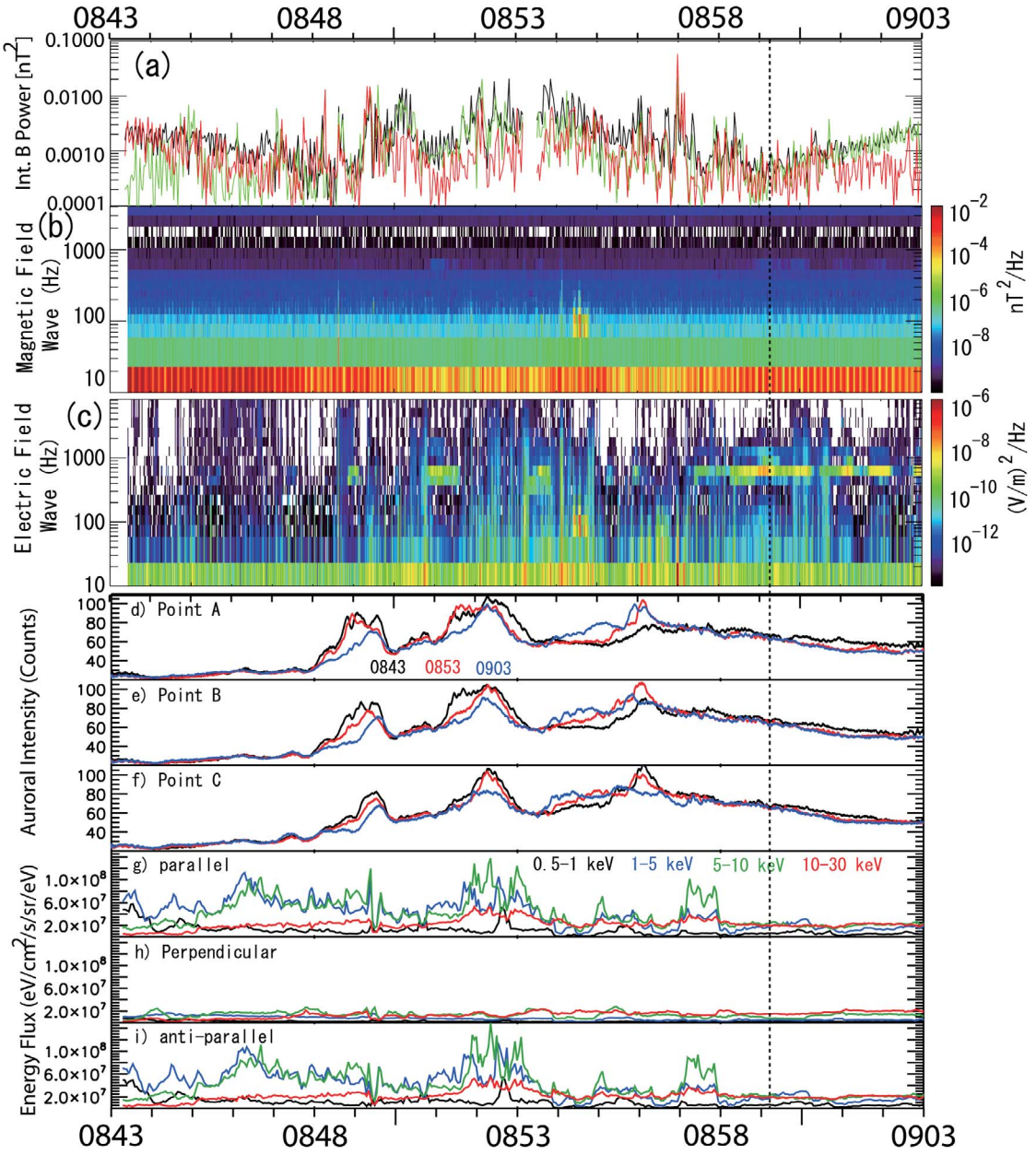

Figure 8. (a) Integrated wave power and (b) magnetic and (c) electric field wave spectra observed by THD. Black, green, and red curves in Figure 8a are Bx (earthward), By (Bx × Bz), and Bz (parallel) in magnetic field-aligned coordinates. Auroral intensity in unit of counts at footprints of (d) A, (e) B, and (f) C in Figure 7 during 0845-0910 UT. Black, red, and blue curves indicate counts at footprints of three times Figures 8a–8c (0843, 0853, and 0903 UT), respectively. Electron-energy flux of (g) field-aligned downward (0°–20°), (h) perpendicular (80°–100°), and (i) field-aligned upward (160°–180°) obtained from the THD-ESA observation. The fluxes are categorized according to electron energy of 0.5–1 keV (black), 1–5 keV (blue), 5–10 keV (green), and 10–30 keV (red). The vertical dashed line denotes the time when wave observations with the highest time resolution were performed by THD, as shown in Figure 11.

pulsations and the fluctuations of energy flux observed by THD, Figure 9 shows frequency spectra obtained by taking the Fast Fourier Transform (FFT) of the auroral intensity and electron flux data in Figure 8. The auroral intensities in Figure 8, averaged over the three temporal footprints (a–c), are indicated by three thin-solid curves in Figure 8 for three IMF-Bz footprints (A), (B), and (C). For the electron fluxes, the spectra of field-aligned downward electrons with energies of 1–5, 5–10, and 10–30 keV, and the upward electrons with energy of 5–10 keV are plotted.

[28] In the three auroral intensity spectra, a pronounced peak is seen at ~0.1 Hz (10 s), as shown by the white arrow. The spectra at 0.13–0.2 Hz (5–8 s) are also enhanced. These power enhancements indicate that an auroral pulsation with a period of 5–10 s occurred at the possible footprints of THD. For the electron flux data, such a significant peak is

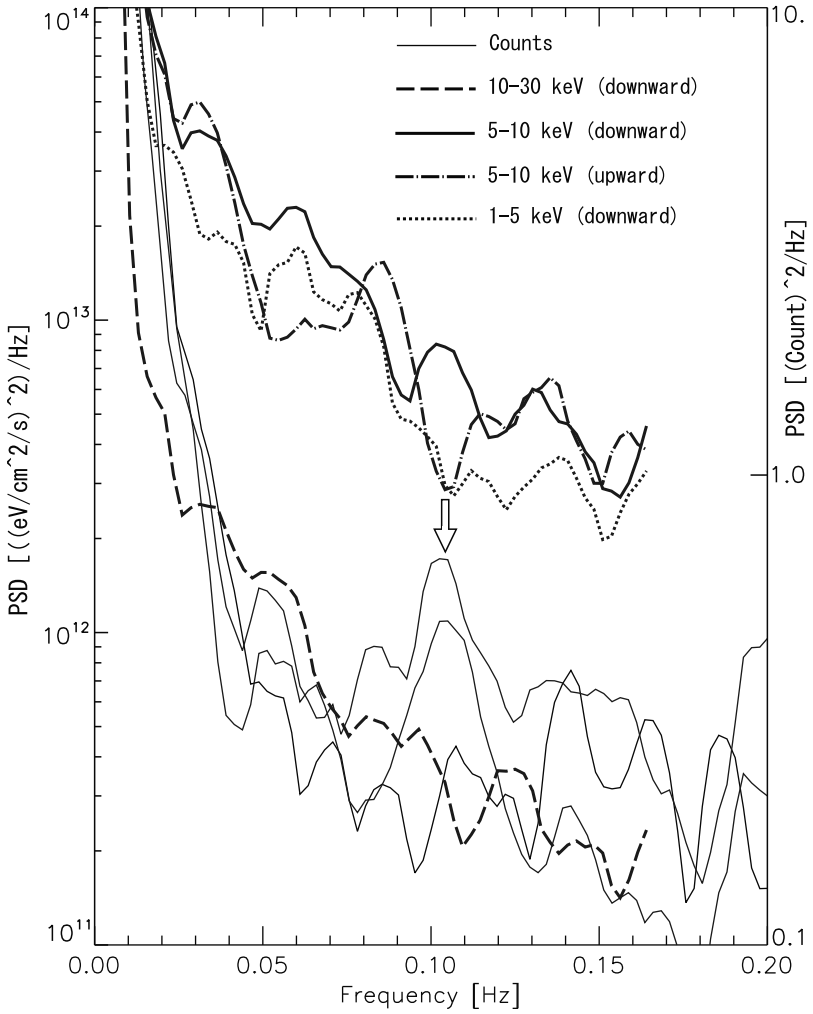

Figure 9. Power spectral density (PSD) obtained through Fast Fourier Transform for the auroral intensities in Figures 8d–8f (thin solid curves) and the electron fluxes in Figures 8g–8i at frequencies of 0.0–0.2 Hz.

not seen. Power enhancements can be recognized at 0.10–0.15 Hz (7–10 s) for all the electron-flux spectra. A small spectral peak at 0.85 Hz is also identified in the spectrum of the upward electron flux of 5–10 keV. Since the THEMIS electron detector may intermittently observe the loss cone, fluctuation of the electron flux synchronized with relative variations between the satellite and ambient magnetic field may also be embedded in these power spectra of electron fluxes.

[29] Whistler mode chorus emissions possibly contribute to pulsating auroras through pitch angle scattering of plasma sheet electrons near the equatorial plane [e.g., *Johnstone*, 1983]. To investigate the possibility of wave-particle interaction during the pulsating aurora event of 8 January 2008, we compare the electron data obtained by ESA with wave data obtained by SCM and EFI. In addition to the wave data from FBK (in Figures 5g and 5h) with lower-frequency resolution, magnetic field observations by SCM with a time resolution of 128 Hz were performed at 0843-0903 UT when the electrons were observed by ESA with the highest time resolution.

[30] Figure 10 shows the energy fluxes of field-aligned downward electrons with energies of 1–5 and 5–10 keV and wave power observed by FBK and SCM at 0847-0854 UT. The wave power enhancements at 0848:28-0848:45 UT in Figures 10b and 10c are due to instrumental noise.

[31] The frequency ranges in Figures 10b and 10c are selected based on the scenario that pulsating auroras are caused by pitch angle scattering through whistler wave-particle interactions near the equatorial plane of the magnetosphere [e.g., *Johnstone*, 1983]. Whistler mode chorus emissions are characterized as having lower-band (0.1–0.5f_{ce}) and upper-band (0.5–0.8f_{ce}) frequency ranges [e.g., *Santolík et al.*, 2003]. During the time period shown in Figure 10, the electron cyclotron frequency (f_{ce}) is ~300–500 Hz. The wave power (magnetic field) for the three frequencies of 9, 36, and 140 Hz below 0.8f_{ce} obtained from FBK is plotted in Figure 10b. From a Fast-Fourier-Transform of the 128-Hz sampled SCM data, Figure 10c shows wave power with frequencies of 31–64 Hz. While 64 Hz is the upper-limit frequency from the SCM data (the Nyquist frequency), the range 31–64 Hz corresponds to frequency of

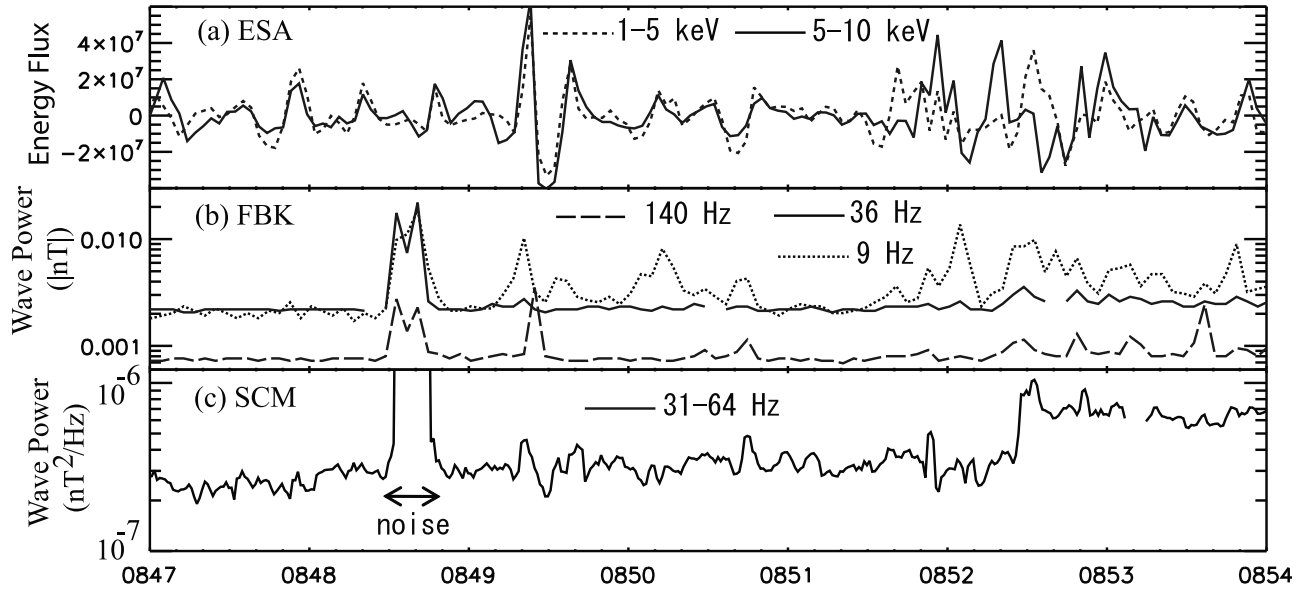

Figure 10. (a) Energy fluxes of field-aligned downward electrons (0°–20°) at energies of 1–5 keV (dotted curve) and 5–10 keV (solid curve) during 0847-0854 UT. (b) Wave power with frequencies of 9 Hz (dotted curve), 36 Hz (solid curve), and 140 Hz (dashed curve) obtained by FBK. (c) Wave power with frequencies of 31–64 Hz obtained from 128-Hz sampled SCM data.

$\sim$0.1–0.2f_{ce} in the case of $f_{ce}\sim$300 Hz, being a part of the lower-band chorus intensity.

[32] Clear correlation cannot be made between the electron fluxes in Figure 10a and the wave powers in Figures 10b and 10c. The wave power is less than 0.01 nT in the FBK data and less than 10^{-6} nT^2/Hz in the SCM data, which are weaker than typical whistler mode chorus waves.

[33] During the present pulsating aurora event, electric and magnetic fields were observed by EFI and SCM with the highest time resolution of 8 kHz for 8-s intervals at (1) $\sim$0847 UT, (2) $\sim$0849 UT, (3) $\sim$0859 UT, and (4) $\sim$0901 UT. During these 8-s measurements, the electron pitch angle distributions were observed by ESA every 3 s. Since timing (1) is before the electron flux enhancement and timing (2) was contaminated by instrumental noise, we show pitch angle and field characteristics at timing (3) in Figure 11. Shown are the pitch angle distributions of electrons at 0859:07-0859:10 UT (Figure 11a) and 0859:10-0859:13 UT (Figure 11b) and the wave spectrogram for X component of the electric (Figure 11c) and magnetic (Figure 11d) fields at frequencies over 1.0 Hz–10 kHz during 0859:05-0859:14 UT. Timing (3) is indicated by vertical dashed lines in Figures 5 and 8.

[34] Field-aligned electron fluxes over $\sim$1–10 keV are larger than the perpendicular fluxes. A clear peak is not identified at a particular energy in the electron distributions in Figures 11a and 11b. In Figures 11c and 11d, the ECH wave is seen as a discrete wave at $f\sim$700 Hz and weaker waves at $\sim$1.1 kHz ($(n + 1/2)f$), above f_{ce} ($\sim$540 Hz) mainly in the electric field data. Continuous whistler mode waves are observed below a few hundred Hz in Figures 11c and 11d. However, their power is not so large ($\sim 10^{-4}$ (mV/m)^2/Hz at 10–100 Hz and $\sim 10^{-2}$ (mV/m)^2/Hz at <10 Hz in the electric field and $10^{-6} - 10^{-7}$ nT^2/Hz at 10–100 Hz and $10^{-5} - 10^{-6}$ nT^2/Hz at <10 Hz in the magnetic field). Similar pitch angle and field characteristics are observed at timing (4) at $\sim$0901 UT.

3. Discussion

[35] For the pulsating aurora event on 8 January 2008, the THD satellite was located at the conjugate magnetosphere in the equatorial plane, according to the field-line mapping using the T96_01 magnetic field model. Since the pulsating aurora covered the entire sky of Gillam after 0850 UT, we consider that the THD was at least in the source region of some patch of the pulsating auroras despite the ambiguity of field-line mapping. The variation in field-aligned electron fluxes shows positive correlations with the observed auroral intensity variation, supporting the idea that the THD was near the conjugate point of the pulsating aurora, although a significant spectral peak was not seen in the electron fluxes.

[36] The observed electron flux was highly field-aligned, as shown in Figures 5, 6, and 11. These field-aligned electron beams are probably not the ionospheric secondary electrons generated by collision between precipitating electrons and the neutral atmosphere. These secondary electrons move upward due to the magnetic mirror force and can be observed as a field-aligned electron beam in the magnetosphere. However, such secondary electrons usually have energies below 1 keV [e.g., *Evans*, 1974]. On the other hand, the field-aligned electron beam was observed at energies of 1–10 keV for the present event.

[37] The observed field-aligned distribution of plasma sheet electrons is similar to those typically observed associated with field dipolarization and earthward high-speed ion flow (bursty bulk flow) at substorm onset, as reported by *Shiokawa et al.* [2003]. *Hada et al.* [1981] suggested that

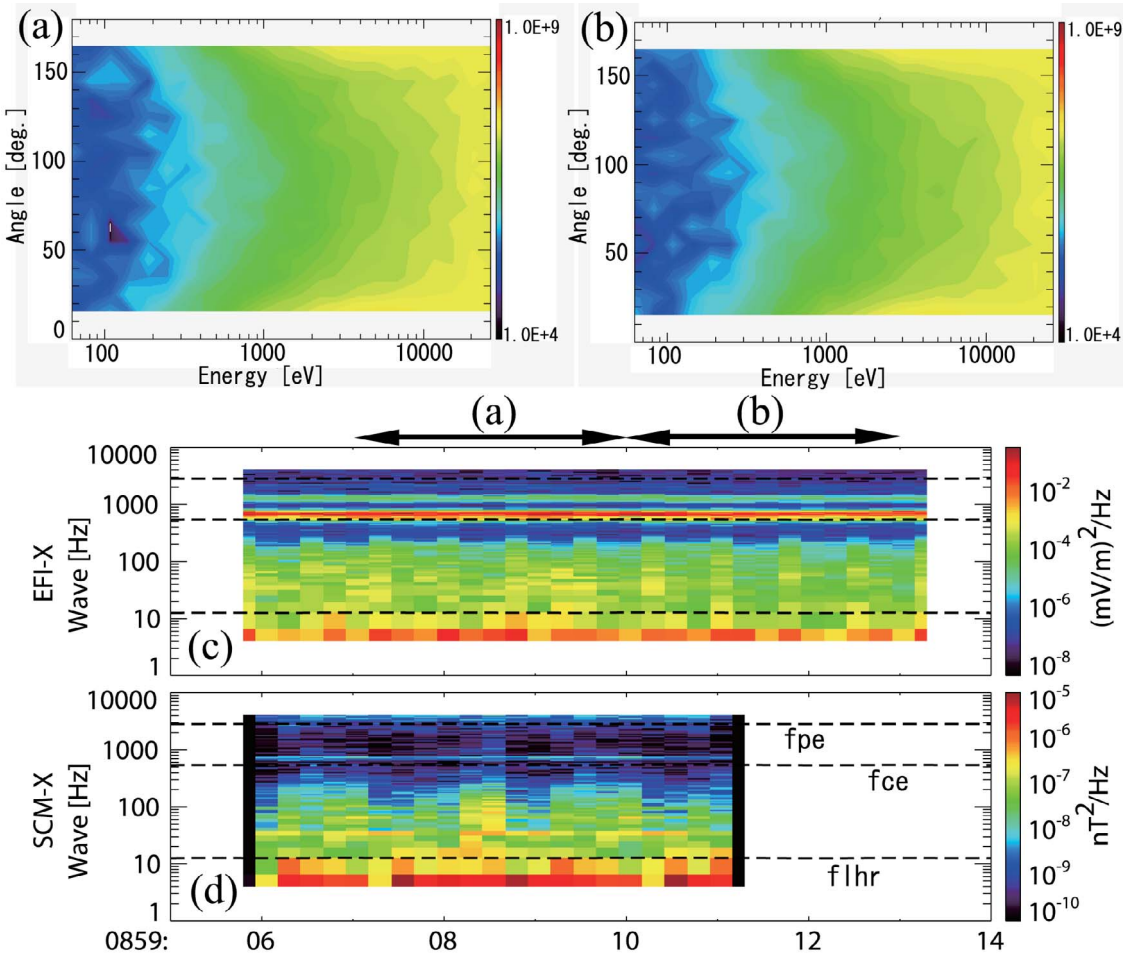

Figure 11. Pitch angle distributions using differential-electron energy flux as functions of energy and pitch angle obtained by ESA at (a) 0859:07-0859:10 UT and (b) 0859:10-0859:13 UT. These times are indicated by horizontal black arrows in Figure 11c. Wave spectrogram for X component of the (c) electric and (d) magnetic fields at frequencies of 1.0 Hz–10 kHz during 0859:05-0859:14 UT. During this time duration, the electric and magnetic field data observed by EFI and SCM with the highest time resolution of ~8 kHz. In Figures 11c and 11d, plasma frequency (f_{pe}), electron cyclotron frequency (f_{ce}), and lower hybrid resonance frequency (f_{lhr}) are indicated from top to bottom by the dashed lines.

these electrons are caused by Fermi-type field-aligned electron acceleration in the neutral sheet.

[38] The observed field-aligned electrons are very different from ordinary expectations in the magnetospheric source region of pulsating auroras. If one considers that the scattering of electrons by whistler mode waves generates pulsating auroras, electron temperature anisotropy with higher temperature in perpendicular direction is necessary to excite whistler mode waves [e.g., *Sagdeev and Shafranov*, 1961; *Andronov and Trakhtengerts* 1964; *Kennel and Petschek*, 1966].

[39] During the present event, however, whistler mode waves are weakly observed in the wave spectra in Figures 5, 6, 8, and 11. Considering the cyclotron resonance condition with the observed magnetic field and plasma density data, the whistler mode waves at ~50–300 Hz can interact with the observed 1–10 keV electrons for the present case. The wave power at this frequency range is $\sim 10^{-4}$ $(\mathrm{mV/m})^2/\mathrm{Hz}$ in the electric field and $10^{-6} - 10^{-7}$ $\mathrm{nT}^2/\mathrm{Hz}$ in the magnetic field, as shown in Figures 8, 10 and 11. These values are one order smaller than those reported by *Nishimura et al.* [2010], which showed clear correlation between whistler wave bursts and auroral pulsations. Clear correlation between the wave power variations and field-aligned electron energy fluxes and/or auroral intensity is also not seen in Figures 8 and 10 for this frequency range.

[40] In order to estimate the loss timescales, we evaluate the decay rates τ_* due to whistler mode waves along the drift path using the approximated formula of *Albert and Shprits* [2009] with the quasi-linear pitch angle diffusion coefficients [*Albert*, 1999]. The observed wave amplitude, wave-spectrum, and f_p/f_{ce} are used for the calculation. The decay rate τ_* [s] is given by

$$\tau_* = \int_{\alpha_L}^{\pi/2} \frac{1}{2D_{\alpha\alpha}(\alpha)\tan\alpha} d\alpha, \qquad (1)$$

where $D_{\alpha\alpha}(\alpha)$ is the bounce-averaged pitch angle diffusion coefficient, and α_L is the loss cone angle.

[41] The total loss timescale τ [s] is given by [*Chen and Schulz*, 2001]

$$\tau = \frac{\tau_* D_{SD} + 1}{D_{SD}} \quad (2)$$

where D_{SD} is the strong diffusion limit by *Summers and Thorne* [2003]. The strong diffusion life time of 10 keV is about 1.0×10^5 s, while τ_* is about 2.0×10^6 s. Therefore, τ is about 2.0×10^6 s, which is much longer than typical precipitation timescale of the inner magnetosphere [*Kurita et al.*, 2011]. Therefore, the observed whistler mode waves are too weak to cause significant precipitation of electrons.

[42] The low-frequency waves below f_{lhr} (~8–13 Hz) which would be magnetosonic mode waves [e.g., *Horne et al.*, 2007], were observed continuously from 0850 to 0900 UT in Figure 5. The integrated wave power in Figure 8a, which is mainly from these low-frequency waves, shows positive correlation with the auroral intensity and field-aligned electron flux. From the FBK data in Figure 10, wave power with a frequency of 9 Hz, which is lower than $0.1 f_{ce}$, tends to be more sensitive to the fluctuation of the 1–10 keV electron energy flux than the other frequencies (36 and 140 Hz). The low-frequency waves below f_{lhr}, however, resonate with electrons above 30 keV, which is higher than the energy range (1–10 keV) of the observed fluctuation of electron flux.

[43] In the wave spectra in Figures 8 and 11, clear discrete waves were observed at $f \sim 700$ Hz with weaker waves at ~1.1 kHz ($\sim (n + 1/2)f$) above the local electron cyclotron frequency f_{ce} (~540 Hz) mainly in the electric field, indicating that they are possibly electrostatic cyclotron harmonic (ECH) waves. Several previous studies of wave-particle interaction showed that not only the whistler waves but also ECH waves can resonate with electrons for the diffuse aurora [e.g., *Horne et al.*, 2003; *Nishimura et al.*, 2010; *Liang et al.*, 2010, 2011a, 2011b; *Ni et al.*, 2012]. *Horne et al.* [2003] showed that ECH waves scatter electrons in the 0.1 keV to a few keV energy range. The pitch angle diffusion coefficient tends to have large value in lower energy [*Horne and Thorne*, 2000]. More recently, *Thorne et al.* [2010] derived pitch angle diffusion coefficients for lower-/upper band chorus as well as ECH waves and concluded that chorus waves are the primary scattering mechanism for diffuse aurora precipitations. By putting the observed f_p and f_{ce} and electron temperature (4 keV) into the dispersion relation of ECH waves and assuming wave propagation angle to be 89°, we found that the observed discrete waves at 700 Hz and 1.1kHz cannot interact with electrons via the first-order cyclotron resonance [e.g., *Horne et al.*, 2003]. The weaker waves near f_{ce} (540 Hz) can interact with 0.1–1 keV electrons, which is lower than the typical energy of electrons responsible for pulsating auroras.

[44] From these considerations, the typical scenario of pulsating auroras, i.e., scattering of electrons by whistler mode waves and/or ECH waves as clearly indicated by *Nishimura et al.* [2010], may not be relevant for the present pulsating aurora event. It is noteworthy that the present THEMIS observations were made at radial distances of 11.6–11.8 R_E which are greater than those of *Nishimura et al.* [2010, 2011], 5–9 R_E. The MSP data in Figure 3 clearly shows that the observed aurora was located at the poleward part of the proton aurora. These facts indicate that the present event is occurring in the mid-tail plasma sheet. Different mechanisms may cause pulsating auroras at higher latitudes.

[45] As a possible explanation of the present event, we suggest that the observed field-aligned electrons, probably caused by Fermi-type accelerations associated with earthward plasma flow, are modulated by the observed weak whistler mode waves, ECH waves, and/or magnetosonic waves, which are candidates for the modulation of electron fluxes and thus pulsating auroras. The field-aligned electrons observed during the present event are not favorable to the generation of whistler and ECH waves through the electron temperature anisotropy. Whistler and ECH waves were observed weakly during the present event, however. Since the field-aligned electrons are already generated by earthward flow, even small pitch angle modulation around the loss cone angle by weak waves may produce pulsation of auroras. The occurrence rate of this type of field-aligned electrons clearly increases with increasing radial distance from 10 to 20 R_E, as shown by *Shiokawa et al.* [2003]. Thus, such a process would occur at higher latitudes of the auroral oval.

[46] The other possibility is kinetic Alfvén waves, which have periods on order of seconds. Usually the acceleration energy of electrons by kinetic Alfvén waves is less than 1 keV [e.g., *Watt et al.*, 2006]. However if the kinetic Alfvén waves contribute pitch angle scattering of the observed preexisting field-aligned electrons, it may be possible to produce modulation of the electron fluxes at ionospheric altitudes.

[47] From the ground-based observations using 30-Hz sampled ASIs, we feel that the auroras, except for discrete, curtain-like ones, always show some pulsating features even at the initial stage of substorms. Modulation of electron fluxes by waves may occur everywhere in the equatorial plane of the plasma sheet.

4. Summary and Conclusions

[48] We investigated particle and wave characteristics near the magnetic equatorial plane during the pulsating aurora event observed by a 30-Hz sampled ASI at Gillam on 8 January 2008. We based our study on ground and THEMIS observations in the mid-tail region at 11.6–11.8 R_E, much larger radial distances than those of *Nishimura et al.* [2010]. The observations and suggestions of this paper are summarized as follows.

[49] 1. The weak auroral pulsations started at ~0842 UT in the FoV of ASI at Gillam in the post-midnight sector (~2 h MLT). The luminosity of the pulsations became most active over all the FoV at ~0850-0904 UT. Weaker pulsations had been observed with decreasing auroral luminosity until ~1200 UT.

[50] 2. The THD and THE satellites were located near the magnetic equatorial plane at 11.6–11.8 R_E in the post-midnight sector near the geomagnetic conjugate of Gillam. The footprints of THD and THE calculated by T96_01 geomagnetic field model were in the FoV of ASI at Gillam during 0835-0910 UT. The magnetic field intensity and directions are mostly consistent between THD observations and T96_01 model. The footprint of THD was located at the poleward part of the proton aurora during the event.

[51] 3. THD and THE performed particle and field observations with the highest-time resolution during this event. After the onset of auroral pulsation (~0842 UT), both THD and THE observed enhanced field-aligned electron fluxes at energies of 1–10 keV, while perpendicular flux was weak. The field-aligned electron fluxes and their variations observed by THD tend to be large when auroral luminosity is large at the THD footprints. Auroral luminosity fluctuations show a peak at ~0.1–0.2 Hz in their frequency spectra; a similar peak was not clearly seen in the electron spectra.

[52] 4. Continuous observations of electric and magnetic waves through EFI and SCM are available. In addition, 8-kHz sampled EFI and SCM data are available for the four 8-s intervals during the event. In these wave observations, whistler mode waves are weakly observed with a power of $\sim 10^{-4}$ $(\mathrm{mV/m})^2/\mathrm{Hz}$ in the electric field and $10^{-6} - 10^{-7}$ $\mathrm{nT}^2/\mathrm{Hz}$ in the magnetic field for the frequency range of ~50–300 Hz, which can interact with the observed 1–10 keV electrons. These values are one order smaller than those reported by *Nishimura et al.* [2010]. Clear correlation between the wave power variations in this frequency range and field-aligned electron energy fluxes and/or auroral intensity is not seen.

[53] 5. Clear, discrete waves were continuously observed at $f \sim 700$ Hz with weaker waves at ~1.1 kHz ($\sim(n + 1/2)f$) above the local electron cyclotron frequency f_{ce} (~540 Hz), mainly in the electric field, indicating that they are ECH waves. However, it is not likely that the observed ECH waves significantly contribute to the observed fluctuation of electrons at 1–10 keV, since typical resonance energies of ECH waves are much lower than 1 keV.

[54] From these observations, we suggest that the observed field-aligned electrons, which are probably caused by Fermi-type acceleration associated with earthward plasma flow in the mid-tail plasma sheet, are modulated by some wave processes to cause pulsating auroras observed at higher latitudes of the auroral oval. In the observation using 30-Hz ASIs, auroras always tend to show some pulsations, even at the initial phase of substorms. Modulation of electron fluxes by waves may occur everywhere in the equatorial plane of the plasma sheet.

[55] **Acknowledgments.** The observatories at Gillam and Fort Smith are Canadian Geospace Monitoring (CGSM) program core sites operated by the Canadian Space Agency. The campaign was carried out by the Solar-Terrestrial Environment Laboratory, Nagoya University in collaboration with the Canadian Space Agency, and with the support from the NORSTAR team of the University of Calgary. Conjunction Event Finder at DARTS JAXA/ISAS provided useful information for this study. The package of subroutines and source codes for calculation of satellite footprints was obtained from Community Coordinated Modeling Center (CCMC), Goddard Space Flight Center. The French involvement (SCM instruments) on THEMIS is supported by CNES and CNRS-INSU. This work was supported by a Grant-in-Aid for Scientific Research (18403011, 20244080, 23403009); Dynamics of the Sun-Earth-Life Interactive System (G-4, the 21st Century COE program) from the Ministry of Education, Culture, Sports, Science, and Technology of Japan, as well as by a grant from the Research Fellowship from the Japan Society for the Promotion of Science.

[56] Robert Lysak thanks the reviewers for their assistance in evaluating this paper.

References

Albert, J. M. (1999), Analysis of quasi-linear diffusion coefficients, *J. Geophys. Res.*, *104*, 2429–2441.

Albert, J. M., and Y. Y. Shprits (2009), Estimates of lifetimes against pitch angle diffusion, *J. Atmos. Sol. Terr. Phys.*, *71*, 1647–1652.

Andronov, A. A., and V. Y. Trakhtengerts (1964), Instability of one-dimensional packets and absorption of electromagnetic waves in a plasma, *Sov. Phys. JETP*, Engl. Transl., *18*(3), 698–702.

Angelopoulos, V., et al. (2008), First results from the THEMIS mission, *Space Sci. Rev.*, *141*, 453–476, doi:10.1007/s11214-008-9378-4.

Auster, H. U., et al. (2008), The THEMIS fluxgate magnetometer, *Space Sci. Rev.*, *141*, 235–264, doi:10.1007/s11214-008-9365-9.

Bonnell, J. W., et al. (2008), The electric field instrument (EFI) for THEMIS, *Space Sci. Rev.*, *141*, 303–341, doi:10.1007/s11214-008-9469-2.

Chen, M. W., and M. Schulz (2001), Simulations of diffuse aurora with plasma sheet electrons in pitch angle diffusion less than everywhere strong, *J. Geophys. Res.*, *106*, 28,949–28,966.

Davidson, G. T. (1990), Pitch angle diffusion and the origin of temporal and spatial structures in pulsating aurorae, *Space Sci. Rev.*, *53*, 45–82.

Evans, D. S. (1974), Precipitating electron fluxes formed by a magnetic field aligned potential difference, *J. Geophys. Res.*, *79*(19), 2853–2858.

Fujii, R., N. Sato, T. Ono, H. Fukunishi, T. Hirasawa, S. Kokubun, T. Araki, and T. Saemundsson (1987), Conjugacies of pulsating auroras by all-sky TV observations, *Geophys. Res. Lett.*, *14*(2), 115–118.

Hada, T., A. Nishida, T. Terasawa, and E. W. Hones Jr. (1981), Bidirectional electron pitch angle anisotropy in the plasma sheet, *J. Geophys. Res.*, *86*, 211–224.

Horne, R. B., and R. M. Thorne (2000), Electron pitch angle diffusion by electrostatic electron cyclotron harmonic waves: The origin of pancake distributions, *J. Geophys. Res.*, *105*, 5391–5402.

Horne, R. B., R. M. Thorne, N. P. Meredith, and R. R. Anderson (2003), Diffuse auroral electron scattering by electron cyclotron harmonic and whistler mode waves during an isolated substorms, *J. Geophys. Res.*, *108*(A7), 1290, doi:10.1029/2002JA009736.

Horne, R. B., R. M. Thorne, S. A. Glauert, N. P. Meredith, D. Pokhotelov, and O. Santolík (2007), Electron acceleration in the Van Allen radiation belts by fast magnetosonic waves, *Geophys. Res. Lett.*, *34*, L17107, doi:10.1029/2007GL030267.

Johnstone, A. D. (1983), The mechanism of pulsating aurora, *Ann. Geophys.*, *1*, 397–410.

Kennel, C., and H. Petschek (1966), Limit on stably trapped particle fluxes, *J. Geophys. Res.*, *71*(1), 1–28.

Kurita, S., et al. (2011), Transport and loss of the inner plasma sheet electrons: THEMIS observations, *J. Geophys. Res.*, *116*, A03201, doi:10.1029/2010JA015975.

Li, W., R. M. Thorne, J. Bortnik, Y. Nishimura, and V. Angelopoulos (2011a), Modulation of whistler mode chorus waves: 1. Role of compressional Pc4–5 pulsations, *J. Geophys. Res.*, *116*, A06205, doi:10.1029/2010JA016312.

Li, W., J. Bortnik, R. M. Thorne, Y. Nishimura, V. Angelopoulos, and L. Chen (2011b), Modulation of whistler mode chorus waves: 2. Role of density variations, *J. Geophys. Res.*, *116*, A06206, doi:10.1029/2010JA016313.

Liang, J., V. Uritsky, E. Donovan, B. Ni, E. Spanswick, T. Trondsen, J. Bonnell, A. Roux, U. Auster, and D. Larson (2010), THEMIS observations of electron cyclotron harmonic emissions, ULF waves, and pulsating auroras, *J. Geophys. Res.*, *115*, A10235, doi:10.1029/2009JA015148.

Liang, J., V. Uritsky, E. Donovan, B. Ni, E. Spanswick, T. Trondsen, J. Bonnell, A. Roux, U. Auster, and D. Larson (2011a), THEMIS observations of electron cyclotron harmonic emissions, ULF waves, and pulsating auroras, *J. Geophys. Res.*, *115*, A10235, doi:10.1029/2009JA015148.

Liang, J., B. Ni, E. Spanswick, M. Kubyshkina, E. F. Donovan, V. M. Uritsky, R. M. Thorne, and V. Angelopolous (2011b), Fast earthward flows, electron cyclotron harmonic waves, and diffuse auroras: Conjunctive observations and synthesized scenario, *J. Geophys. Res.*, *116*, A12220, doi:10.1029/2011JA017094.

McFadden, J. P., et al. (2008), The THEMIS ESA plasma instrument and in-flight calibration, *Space Sci. Rev.*, *141*, 277–302, doi:10.1007/s11214-008-9440-2.

Minatoya, H., T. Ono, N. Sato, K. Makita, and T. Toshino (1995), Development of image data processing system for the conjugate auroral TV data, *Antarct. Res.*, *38*, 113–147.

Miyoshi, Y., Y. Katoh, T. Nishiyama, T. Sakanoi, K. Asamura, and M. Hirahara (2010), Time of flight analysis of pulsating aurora electrons, considering wave-particle interactions with propagating whistler mode waves, *J. Geophys. Res.*, *115*, A10312, doi:10.1029/2009JA015127.

Nemzek, R. J., R. Nakamura, D. N. Baker, R. D. Belian, D. J. McComas, M. F. Thomsen, and T. Yamamoto (1995), The relationship between pulsating auroras observed from the ground and energetic electrons and plasma density measured at geosynchronous orbit, *J. Geophys. Res.*, *100*, 23,935–23,944.

Ni, B., J. Liang, R. M. Thorne, V. Angelopoulos, R. B. Horne, M. Kubyshkina, E. Spanswick, E. F. Donovan, and D. Lummerzheim

(2012), Efficient diffuse auroral electron scattering by electrostatic electron cyclotron harmonic waves in the outer magnetosphere: A detailed case study, *J. Geophys. Res.*, *117*, A01218, doi:10.1029/2011JA017095.

Nishimura, Y., et al. (2010), Identifying the driver of pulsating aurora, *Science*, *330*(6000), 81–84, doi:10.1126/science.1193186.

Nishimura, Y., et al. (2011), Estimation of magnetic field mapping accuracy using the pulsating aurora]chorus connection, *Geophys. Res. Lett.*, *38*, L14110, doi:10.1029/2011GL048281.

Nishiyama, T., T. Sakanoi, Y. Miyoshi, Y. Katoh, K. Asamura, S. Okano, and M. Hirahara (2011), The source region and its characteristic of pulsating aurora based on the Reimei observations, *J. Geophys. Res.*, *116*, A03226, doi:10.1029/2010JA015507.

Oguti, T. (1978), Observations of rapid auroral fluctuations, *J. Geomagn. Geoelectr.*, *30*, 299–314.

Roux, A., et al. (2008), The search coil magnetometer for THEMIS, *Space Sci. Rev.*, *141*, 265–275, doi:10.1007/s11214-008-9455-8.

Royrvik, O., and T. N. Davis (1977), Pulsating aurora: Local and global morphology, *J. Geophys. Res.*, *82*, 4720–4740.

Sagdeev, R. D., and V. D. Shafranov (1961), On the instability of a plasma with an anisotropic distribution of velocities in a magnetic field, *Sov. Phys. JETP*, Engl. Transl., *12*(1), 130–132.

Sakaguchi, K., K. Shiokawa, A. Ieda, R. Nomura, A. Nakajima, M. Greffen, E. Donovan, I. R. Mann, H. Kim, and M. Lessard (2009), Fine structures and dynamics in auroral initial brightening at substorm onsets, *Ann. Geophys.*, *27*, 623–630.

Sandahl, I., L. Eliasson, and R. Lundin (1980), Rocket observations of precipitating electrons over a pulsating aurora, *Geophys. Res. Lett.*, *7*, 309–312.

Santolík, O., D. A. Gurnett, J. S. Pickett, M. Parrot, and N. Cornilleau-Wehrlin (2003), Spatio-temporal structure of storm-time chorus, *J. Geophys. Res.*, *108*(A7), 1278, doi:10.1029/2002JA009791.

Sato, N., D. M. Wright, Y. Ebihara, M. Sato, Y. Murata, H. Doi, T. Saemundsson, S. Milan, M. Lester, and C. W. Carlson (2002), Direct comparison of pulsating aurora observed simultaneously by the FAST satellite and from the ground at Syowa, *Geophys. Res. Lett.*, *29*(21), 2041, doi:10.1029/2002GL015615.

Sato, N., D. M. Wright, C. W. Carlson, Y. Ebihara, M. Sato, T. Saemundsson, S. Milan, and M. Lester (2004), Generation region of pulsating aurora obtained simultaneously by the FAST satellite and a Syowa-Iceland conjugate pair of observations, *J. Geophys. Res.*, *109*, A10201, doi:10.1029/2004JA010419.

Shiokawa, K., W. Baumjohann, and G. Paschmann (2003), Bi-directional electrons in the near-Earth plasma sheet, *Ann. Geophys.*, *21*, 1497–1507.

Shiokawa, K., et al. (2009), Longitudinal development of a substorm brightening arc, *Ann. Geophys.*, *27*, 1935–1940.

Summers, D., and R. M. Thorne (2003), Relativistic electron pitch-angle scattering by electromagnetic ion cyclotron waves during geomagnetic storms, *J. Geophys. Res.*, *108*(A4), 1143, doi:10.1029/2002JA009489.

Thorne, R. M., B. Ni, X. Tao, R. B. Horne, and N. P. Meredith (2010), Scattering by chorus waves as the dominant cause of diffuse auroral precipitation, *Nature*, *467*, 943–946, doi:10.1038/nature09467.

Tsuruda, K., S. Machida, T. Oguchi, S. Kokubun, K. Hayashi, T. Kitamura, O. Saka, and T. Watanabe (1981), Correlations between the very low frequency chorus and pulsating aurora observed by low-light-level television at L∼4.4, *Can. J. Phys.*, *59*, 1042–1048.

Tsyganenko, N. A. (1995), Modeling the Earth's magnetospheric magnetic field confined within a realistic magnetopause, *J. Geophys. Res.*, *100*, 5599–5612.

Tsyganenko, N. A. (1996), Effects of the solar wind conditions on the global magnetospheric configuration as deduced from data-based field models, in *Third International Conference on Substorms (ICS-3)*, edited by E. Rolfe and B. Kaldeich, *Eur. Space Agency Spec. Publ.*, *ESA SP-389*, 181–185.

Watanabe, M., A. Kadokura, N. Sate, and T. Saemundsson (2007), Absence of geomagnetic conjugacy in pulsating auroras, *Geophys. Res. Lett.*, *34*, L15107, doi:10.1029/2007GL030469.

Watt, C. E. J., R. Rankin, I. J. Rae, and D. M. Wright (2006), Inertial Alfvén waves and acceleration of electrons in nonuniform magnetic fields, *Geophys. Res. Lett.*, *33*, L02106, doi:10.1029/2005GL024779.

Yamamoto, T. (1988), On the temporal fluctuations of pulsating auroral luminosity, *J. Geophys. Res.*, *93*, 897–911.

V. Angelopoulos, Institute of Geophysics and Planetary Physics, University of California, Los Angeles, CA 90024–1567, USA. (vassilis@ucla.edu)

J. W. Bonnell and J. P. McFadden, Space Sciences Laboratory, University of California, Berkeley, CA 94720–7450, USA. (jbonnell@ssl.berkeley.edu; mcfadden@apollo.ssl.berkeley.edu)

E. Donovan, Department of Physics and Astronomy, University of Calgary, AB T2N 1N4, Canada (edonovan@ucalgary.ca)

K.-H. Fornacon, Institut für Geophysik und Meteorologie, Technical University of Braunschweig, Braunschweig D-38106, Germany. (khf@tu-bs.de)

O. Le Contel, Laboratoire de Physique des Plasmas, CNRS-Ecole Polytechnique-UPMC, Palaiseau F-91128, France. (olivier.lecontel@lpp.polytechnique.fr)

S. Lee, Y. Miyoshi, and K. Shiokawa, Solar-Terrestrial Environment Laboratory, Nagoya University, Chikusa-ku, Nagoya 464-8601, Japan. (selee@stelab.nagoya-u.ac.jp; miyoshi@stelab.nagoya-u.ac.jp; shiokawa@stelab.nagoya-u.ac.jp)

A. Nakajima, Japan Science and Technology Agency, 5-7, Chiyoda-ku, Tokyo 102-0076, Japan. (akimitsu@stelab.nagoya-u.ac.jp)

K. Sakaguchi, National Institute of Information and Communications Technology, 4-2-1 Nukui-Kitamachi, Koganei, Tokyo 184-8795, Japan. (kaoris@nict.go.jp)